

DynPL-SVO: A New Method Using Point and Line Features for Stereo Visual Odometry in Dynamic Scenes

Xiaoguang Ma^{*}, Ya Wang^{*}, Baosheng Zhang, Hong-Jun Ma and Chunbo Luo

Abstract—Stereo visual odometry is widely used where a robot tracks its position and orientation using stereo cameras. Most of the approaches recovered mobile robotics motion based on the matching and tracking of point features along a sequence of stereo images. But in low-textured and dynamic scenes, there are no sufficient robust static point features for motion estimation, causing lots of previous work to fail to reconstruct the robotic motion. However, line features can be detected in such low-textured and dynamic scenes. In this paper, we proposed DynPL-SVO, a stereo visual odometry with the *dynamic grid* algorithm and the cost function containing both vertical and horizontal information of the line features. Stereo camera motion was obtained through Levenberg-Marquard minimization of re-projection error of point and line features. The experimental results on the KITTI and EuRoC MAV datasets showed that the DynPL-SVO had a competitive performance when compared to other state-of-the-art systems by producing more robust and accurate motion estimation, especially in low-textured and dynamic scenes.

Index Terms—Dynamic scenes, motion estimation, line feature, visual odometry (VO).

I. INTRODUCTION

VISUAL odometry is an emerging and hot research topic in the fields of robotics, autonomous driving and augmented reality. It usually uses a variety of cameras for mobile robotic motion estimation and also combined with other kinds of sensors, such as IMU, wheel odometry, and so on [1] [2] [3] [4] [5]. Most systems [6] [7] used points as the only visual feature to get motion estimation since points are easy to detect and track, and convenient to handle. Popular point feature

detectors include oriented FAST and rotated BRIEF(ORB)[8], Scale Invariant Feature Transform(SIFT) [9], and Speeded Up Robust Features(SURF), etc. Most methods used ORB as a point feature detector because of its accuracy and speed. But in low-texture scenes, systems with only point features can worsen the performance, since it is difficult to find enough reliable point features in an image. In contrast, line segments are usually abundant in any human-made environment, even in low-texture scenes. In addition, the line segment can provide more structural information for motion estimation.

The process of detecting and describing line segments can be handled by Line Segment Detector(LSD) [10] and Line Band Descriptor(LBD) [11], respectively. Line segments with rich structural information can improve the accuracy and robustness of motion estimation. The *Plücker* coordinates of the line had been proposed by Sola [12] to transform and project efficiently, however, over-parameterization of the spatial line will induce gauge freedom and internal consistency constraints [13]. To apply unconstrained optimization, Bartoli [14] proposed the orthonormal representation of lines with a minimum of four parameters, while still having a good performance.

The Jacobian plays an important role in estimating the mobile robotics motion through least-square minimization of the re-projection error between projected and detected features. The Jacobian of the proposed system includes three cost functions, i.e. 1) the distance from projected point features from the previous frame to matched point features in the current frame; 2) the distance between the endpoints of the matched line in the current frame and the projected infinite line from the previous frame; 3) the distance from the midpoints of matched lines to the midpoints of the projected lines. The Jacobians with the above-mentioned cost functions can make the best use of structural information from both point and line features.

A large number of state-of-the-art visual odometry methods are used in real-time and show promising results with high accuracy. However, all these methods [2] [15] [16] can only work well in static scenes. The real-world environment has not only numerous low-textured scenes but also contains a huge number of highly dynamic scenes. Features attached to dynamic objects could reduce the robustness and accuracy of the system. When dealing with dynamic and complex scenes, the traditional method can not get correct inter-frame matching, resulting in greatly reduced motion estimation accuracy. The idea to solve the above problem is to accurately remove

Xiaoguang Ma is with the State Key Laboratory of Synthetical Automation for Process Industries, Northeastern University, Shenyang 110819, the Foshan Graduate School, Northeastern University, Foshan 528311, China. and College of Information Science and Engineering, Northeastern University, 110819 Shenyang, China (e-mail: maxg@mail.neu.edu.cn).

Ya Wang is with the Department of Cognitive Systems, University of Tuebingen, Sand 1, Tuebingen 72076, Germany (e-mail: francis.wang@uni-tuebingen.de).

Baosheng Zhang is with the College of Information Science and Engineering, Northeastern University, Shenyang 110819, China (e-mail: zhang-baosheng0503@163.com).

Hong-Jun Ma is with the School of Automation Science and Engineering, South China University of Technology, Guangzhou 510641, China, and also with the Key Laboratory of Autonomous Systems and Networked Control, Ministry of Education, Unmanned Aerial Vehicle Systems Engineering Technology Research Center of Guangdong, Guangzhou 510640, China (Hong-Jun Ma is the corresponding author, e-mail: mahongjun@scut.edu.cn).

Chunbo Luo is with the School of Information and School of Information and Communication Engineering, University of Electronic Science and Technology of China, Chengdu 611731, China (e-mail: c.luo@uestc.edu.cn).

^{*} These authors have contributed equally to this work.

the outliers in images before pose optimization, i.e., the system must remove the features introduced by the dynamic objects and rely only on trusted static features for motion estimation. Therefore, how to accurately extract moving objects and remove the dynamic features is critical to improve the performance of visual odometry (VO) systems.

In this paper, we propose DynPL-SVO, a robust visual odometry system using both point and line features with a novel cost function. Our proposed method mainly solves two issues in the VO/visual simultaneous localization and mapping (vSLAM) systems. On one hand, in low-textured scenes, traditional *point-only* VO systems can not detect a large set of point features for motion estimation, so more structural information of point and line features is needed to improve its performance. In the pose optimization, the line segment optimization converts into point feature optimization, which simply solves the line feature optimization issue, we further derived the analytical Jacobian of the line re-projection error. On the other hand, to solve the issue that dynamic scenes reduce the accuracy of VO by using the motion model combines with the dynamic grids to mark dynamic regions and remove dynamic features inside the marked regions before pose optimization.

There are mainly four contributions for the paper.

- We proposed a complete stereo visual odometry system DynPL-SVO using both point and line features, which can cope with dynamic scenes using only stereo RGB images directly from stereo cameras.
- In pose optimization, we used more structural information of line features. The vertical and horizontal re-projection error of line features and the re-projection error of point features were both used to construct a unified cost function, and we further derived the analytical Jacobians of the line re-projection error.
- An effective and fast algorithm was used to remove the outliers using motion model and dynamic grids for visual odometry to solve the problem where dynamic scenes greatly reduced estimation accuracy.
- We conducted extensive comparative experiments on the KITTI dataset for ground vehicles and the EuRoC MAV dataset for aerial vehicles.

II. RELATED WORK

There are many research fields about visual odometry due to its wide scope of applications, and the visual sensors used mainly include monocular cameras, stereo cameras and RGB-D sensors. Monocular cameras are not as good as stereo systems in initialization and estimation accuracy [1] [17]. The RGB-D camera system can directly obtain the depth information of pixels. However, its application range is limited for outdoor scenes [18] [19]. In the past decades, researchers [6] [7] paid more attention to stereo visual odometry because of its low cost, robustness and wide range of applications for both indoor and outdoor scenes.

Visual odometry methods can be divided into *direct-based* [20] [21] and *indirect-based (feature-based)* [6] according to visual measurement processing. There are many *feature-based* works, which usually detect a large set of features in

images, such as ORB points. Compared to the *feature-based* methods, the *direct-based* method directly uses intensity for each pixel to compute the camera motion by minimizing photometric errors, instead of detecting and matching features. However, most of the researchers used *feature-based* ones instead due to its robustness and accuracy of estimation.

Most *feature-based* methods detect and track point features using a feature descriptor. Then they estimate the motion by minimizing the re-projection errors between the corresponding detected and those projected point features from different frames. To ensure the real-time and reliability of the system, many point *feature-based* researches used the ORB method. These VO systems with only point features can obtain robust and accurate motion estimation in rich-texture scenes. But when facing scenes with poor information or harsh weather, such as a foggy environment, the motion estimation accuracy could degrade significantly. To achieve more robust and better accuracy performance, many researchers introduced line features to improve feature detection capability in the low-texture environment [16] [22] [23].

In order to introduce line features into VO/vSLAM, the first thing we need to do is to detect and match line features in the images. Many researchers achieved good results in line features extraction, such as FLD [24], EDLine [25] and Line Segment Detector(LSD) [10]. Among the above-mentioned methods, LSD is significantly better than other straight-line features detection methods in shortening straight lines and in blurred images. Therefore, we used LSD as a line segment detector from stereo images and Line Band Descriptor(LBD) [11] for line description.

How to represent a line segment in the system has always been a key issue in feature extraction, and the most intuitive and concise way is to use two endpoints to model a 3D line as in [26]. Besides, line features can be represented as infinite lines as in [27], utilizing *Plücker* coordinates to represent the infinite line in VO/vSLAM for more convenient projection and transformation of line features. If the position of the spatial lines is used as the key factors to affect the change of the re-projection error, all of the above methods have over-parameterized problems. In order to avoid optimization constraints due to the over-parameterized representation of line features in the optimization process, a lot of work [3] [16] introduced the *Plücker* coordinate representation and the orthogonal representation [14] to realize the line feature transformation and optimization, respectively, instead, we solved the issue by using the Jacobian relationship between the endpoints and the vertical re-projection errors of the line features.

Different representation of the line features needs to design the corresponding cost function for optimization. Koletschka [26] took the euclidean distance sum of equally spaced sampling points on the line segment as the cost function of the line features. Since the endpoints of the line detected by LSD are not stable, the line re-projection error was defined as a vector formed by the euclidean distance from the endpoints of the detected line segment in the current frame and the line projected in the previous frame in most methods [3] [16] [23] [27]. All the above cost functions can be easily formed

by using the *Plücker* coordinate and the distance formula between points and lines. However, these methods only paid attention to structural information in the vertical direction of the line features, ignoring rich structural information in the horizontal direction of the line features. Based on the original cost function, the euclidean distance from the projected midpoints of the line segments in the first frame and the midpoints of the lines detected in the second frame was introduced into the new cost function. Our proposed cost function takes advantage of the structural information in both horizontal and vertical directions of the line features.

Estimating motion in dynamic scenes is also one of the open challenges in visual odometry. To deal with this problem, many methods had been proposed. Some work [4] [5] [28] used vision information to fuse other sensors (such as IMU, wheel odometry, and so on) to reduce the impact of dynamic scenes in motion estimation. In addition, there are a large number of methods [29] [30] using RGB-D information to identify dynamic region. The unstable point features in the dynamic region were eliminated to ensure that only stable static point features were retained in the optimization part. Recently, learning-based computer visual methods are emerging, and also many feasible solutions [31] [32] to handle the impact of dynamic scenes on visual odometry by combining learning methods. However, the above-mentioned solutions all have strict requirements on scenario conditions and computer resources.

In this paper, we propose a stereo visual odometry method that can achieve high accuracy motion estimation without directly using image depth information and other sensor assistance in dynamic scenes.

III. DETECTION AND PRE-PROCESSING

In this section, we mainly introduced the front end of the proposed visual odometer system, including the detection and matching in each stereo image of visual features (point and line segment), the definition of *dynamic grid* and the parameterization of line segments.

A. Feature detection and matching

1) *Point features*: The performance of features detection work will directly affect the running time and motion estimation accuracy. The focus of point features detection is to ensure the real-time performance of the system, while detecting as many stable point features as possible. There are large amount of point features that can be used, like ORB, which is not only fast to compute but also has been verified to be sufficient to meet the need of the system [6]. Therefore, the ORB method was utilized to detect stable point features in the stereo images and describe each detected point feature.

After detecting the point features in left $p_l(u_l, v_l)$ and right $p_r(u_r, v_r)$ images of a stereo frame (see Figure 1), it is required to match point features between the left and right images. We meshed all point features of stereo images, i.e. dividing the image evenly into 64×48 grids and storing all point features according to their grid positions in the image. After that, we used the ORB point feature p_l in the

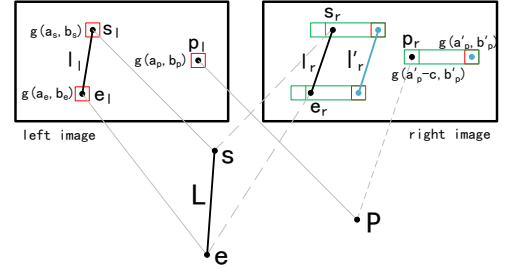


Fig. 1. The feature matching process between the left and right images in the new stereo frame. We assumed that the point p_l detected in the left image in the $grid(a_p, b_p)$ (red square), considering the epipolar constraint and imaging principle of the stereo camera, the point (such as p_r) to be matched in the right image should locate at the range from $grid(a_p - c, b'_p)$ to $grid(a_p, b'_p)$ in the right image, i.e. the green rectangular area. Similar to point matching, the endpoints of the line l_r detected in the right image meet the matching rule. So it will be a candidate line of l_l .

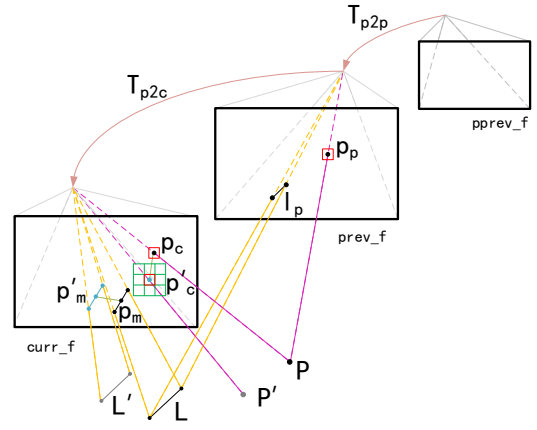


Fig. 2. The feature tracking process between adjacent frames. T_{p2p} denoted the pose transformation between the previous frame $prev_f$ and its previous frame $pprev_f$, T_{p2c} denoted the pose transformation between the $prev_f$ and the current frame $curr_f$. The dynamic spatial point P and spatial line L moved to P' and L' during sampling time. There was a large error between the dynamic matched point features p'_c and the point features p_c estimated by the point features p_p in $prev_f$, we calculated and averaged the sum of squared Euclidean distance between the matched points and the estimated points in all the grids and defined the grid and its surrounding 8 grids in green as *dynamic grid*. For line features L , we used the Euclidean distance between the midpoints (p'_m, p_m) of the matched and estimated line features to find dynamic line features.

$grid(a_p, b_p)$ in the left image to match the point feature p_r in the right image. The feature matching in the stereo camera must follow the epipolar constraint, i.e. $v_l = v_r$, and comply with the imaging principle of the stereo camera, i.e. $u_l > u_r$. The point features to be matched on the right image only include the point features in the horizontal c grids, ranging from $grid(a_p - c, b'_p)$ to $grid(a'_p, b'_p)$ in the right image. This not only greatly improved feature matching efficiency, but also largely avoided the existence of error matching. A mutual consistency check was performed, i.e. the best-left match must correspond to the best-right match, and only these matches were considered valid and used for triangulation.

Figure 2 showed the features tracking process between adja-

cent frames. In order to avoid the influence of a large number of features attached to dynamic objects on the estimation results, we used the motion model, i.e., the pose transformation matrix T_{p2p} between the previous frame $prev_f$ and the $pprev_f$, which denotes the previous frame of the $prev_f$, to estimate the location of the matched point features of p_c in the current frame. Since dynamic objects have more abnormal motion relative to the entire stationary scene, i.e. the dynamic spatial point P moved to P' during sampling time, an intuitive response is that the dynamic features p'_c have a larger re-projection error relative to the features p_c estimated by the motion model. We calculated and averaged the sum of squared Euclidean distance between the matched point features and the estimated point features of the detected point features in all the above grids. Once the value exceeds the threshold, the grid and its surrounding 8 grids in green are determined as *dynamic grid*, and the features in the dynamic grid are dynamic features.

Algorithm 1 showed the detailed process of our proposed dynamic region marking based on the determined *dynamic grid* algorithm.

Algorithm 1 : Dynamic region marking using *dynamic grid*

Input: Motion model T_{p2p} of the previous frame $prev_f$, the matched point feature set between the current frame $curr_f$ and $prev_f$;

Output: The location of the *dynamic grid*.

```

1: Divide  $curr\_f$  evenly into  $64 \times 48$  grids and only keep
    $n(n \leq 8)$  point features  $p_j$  in each grid  $g_i$ ;
2: for each  $g_i \in curr\_f$  do
3:   for each  $p_j \in g_i$  do
4:      $e_{g_i} += PointErr(p_j, T_{p2p})$ 
5:   end for
6:   if  $e_{g_i} > \rho$  then
7:      $GRIDS\_LOCATION += \{(x_{g_i} - 1, y_{g_i} -$ 
8:        $1), (x_{g_i} + 1, y_{g_i} + 1)\}$ 
9:   end if
10: end for
11: return  $GRIDS\_LOCATION$ 

```

2) *Line features*: The detection of line features faces more challenges over that of point features. In real-world scenes, some factors, such as changes of lighting, different point of views, and occlusions make it hard for all detected line features to be stable. The focus of line feature detection is to reduce running time and to improve robustness to light. LSD is a popular line segment detector, widely used in computer vision. It is designed to work on noisy images in various scenes without parameter tuning, and the detected line meets the system requirements in terms of accuracy.

Since the endpoints of the line detected by LSD are not stable, the line cannot be perfectly matched only using its endpoints. Similar to point features matching between the left and right images, we meshed the line features in the right image, i.e. all line features passing through the same grid in the image on the right were managed uniformly. We assumed the grids, where the two endpoints of the line feature l_l in the left image were located in (a_s, b_s) and (a_e, b_e) , and we selected

the line features to be matched within the corresponding grid range in the right image, and only the line l_r meeting the line matching rule will be selected as the candidate line of l_l , as depicted in Figure 1. A mutual consistency check was again performed, i.e. the best-left match must correspond to the best right match, and only these matches that meet the above requirements can participate in the follow-up process.

As shown in Figure 2, for the dynamic line features tracking process between adjacent frames, we used the re-projection error between the estimated line midpoint p_m and the matched line midpoint p'_m as the judgment basis. Once the value exceeded the preset threshold, we determined that the line feature was a dynamic line feature and removed it.

B. Representation of Line Features

A 3D point can be represented by Euclidean spatial coordinates. However, the representation of line features in space is a challenging task. We assumed the homogeneous coordinates of line endpoints are $\bar{X}_s(x_1, y_1, z_1, w_1)$ and $\bar{X}_e(x_2, y_2, z_2, w_2)$, respectively, while their inhomogeneous coordinates were represented as X_s, X_e . Then the *Plücker* coordinates of the line L can be constructed as follows:

$$L = \begin{bmatrix} X_s \times X_e \\ w_2 X_s - w_1 X_e \end{bmatrix} = \begin{bmatrix} \mathbf{n} \\ \mathbf{d} \end{bmatrix} \in \mathbb{R}^6 \quad (1)$$

, where \mathbf{n} and \mathbf{d} are 3-dimensional vectors, \mathbf{d} is the direction vector of the line and \mathbf{n} is the normal vector of the plane determined by the line and the origin, i.e. $\mathbf{n}^T \times \mathbf{d} = 0$. The *Plücker* coordinates L can also be extracted from the dual *Plücker* matrix T^* . The dual plucker matrix can be defined as follows:

$$T^* = \begin{bmatrix} \mathbf{d}^\wedge & \mathbf{n} \\ -\mathbf{n}^T & 0 \end{bmatrix} \quad (2)$$

The representation of *Plücker* coordinates is convenient for both line feature projection and transformation.

In a nutshell, we used the motion model to find the dynamic features, and we used *Plücker* coordinates to parameterize the line features in the proposed visual odometry system. In addition, a simple and effective Jacobian matrix perfectly solved the over-parameterized problem of the *Plücker* coordinates.

IV. MOTION ESTIMATION

In this section, we presented in detail how the point and line measurements were introduced in our system and motion estimation were performed. In addition, we derived the analytical Jacobians of re-projection error with respect to point and line feature parameters.

A. Problem Statement

We had obtained the point and line features in a sequence of images and their plural positions in camera frames. The problem to be solved is how to find the optimal transformation that satisfies projection constraints of the corresponding features as much as possible. This can be solved by a non-linear least-square equation formed by the projection constraints of

the corresponding features in the previous frame and in the current frame.

Different from other point-line VO/vSLAM systems with the re-projection error of point features and with vertical re-projection error of line features, DynPL-SVO not only retained the two kinds of re-projection error above but also introduced the horizontal re-projection error of line features into the motion estimation. This can make full use of the structural characteristics of the line features and improve system robustness and accuracy. So the non-linear least-square equation of our approach is shown in (3).

$$\xi^* = \underset{\xi}{\arg \min} \left[\sum_{i=1}^m e_p^i(\xi)^T \Sigma_{e_p^i}^{-1} e_p^i(\xi) + \sum_{j=1}^n e_{l_v}^j(\xi)^T \Sigma_{e_{l_v}^j}^{-1} e_{l_v}^j(\xi) + \sum_{k=1}^q e_{l_h}^k(\xi)^T \Sigma_{e_{l_h}^k}^{-1} e_{l_h}^k(\xi) \right] \quad (3)$$

, where m, n and q denote the number of points, all lines and the lines whose endpoints are not close to the edge of the image, respectively. It consisted of the point re-projection error e_p^i , vertical and horizontal re-projection error of line feature $e_{l_v}^j, e_{l_h}^k$. The matrices Σ^{-1} in (3) represent the inverse covariance matrices related to the uncertainty of each re-projection error.

The re-projection error of points was defined as the distance between the projected point features from the previous frame to the detected point features in the current frame:

$$e_i^p = p_i - p'_i(\xi) \quad (4)$$

, where $p_i, p'_i(\xi)$ represent point detected from current frame and point projected from the previous frame into current frame, respectively.

Compared with point features, it is a challenging task to introduce the re-projection error of line features into optimization. In most methods, only the vertical re-projection errors of the line features were introduced into the motion estimation, i.e. the distance from the endpoints of the detected line features to the projected infinite line features, shown as

$$e_{l_j}^{l_v} = \begin{bmatrix} d(l_j, p'_{j,s}(\xi)) \\ d(l_j, p'_{j,e}(\xi)) \end{bmatrix} \quad (5)$$

, where p'_s and p'_e denote the endpoints of the line features and $d(\cdot)$ represent the distance function from point to line.

In our method, the horizontal re-projection error of the line features was introduced into the optimization part by using the re-projection error of the midpoints of the line features:

$$e_{l_k}^{l_h} = p_{i,m} - p'_{i,m}(\xi) \quad (6)$$

, where $p_{i,m}, p'_{i,m}(\xi)$ represent midpoint of the line detected from current frame and projected one from previous frame, respectively.

The pose optimization problem in (3) can be iteratively solved using the Gauss-Newton and Levenberg-Marquardt algorithm. To do this, we will illustrate the Jacobian of the three above-mentioned re-projection errors of point and line features in the next section.

B. Jacobian Matrix of Point and Line Re-Projection Errors

1) *Jacobian of point re-projection errors*: In order to derive the Jacobian of feature re-projection error, we converted the pose transformation to Lie algebra form, i.e. using six-dimensional vectors $\xi \in \mathfrak{se}(3)$ to represent the pose transformation matrix $T \in SE(3)$. So the Jacobian of a point features can be expressed as:

$$J_p = \frac{\partial e_i^p}{\partial \delta \xi} = \frac{\partial e_i^p}{\partial P'} \frac{\partial P'}{\partial \delta \xi} \quad (7)$$

, where P' represent 3D point of matched point feature from previous frame in current camera frame. The above Jacobian can be divided into two parts by the chain rule. The first part can be expressed by the camera projection principle as the following equation:

$$\frac{\partial e_i^p}{\partial P'} = - \begin{bmatrix} \frac{\partial u}{\partial X'} & \frac{\partial u}{\partial Y'} & \frac{\partial u}{\partial Z'} \\ \frac{\partial v}{\partial X'} & \frac{\partial v}{\partial Y'} & \frac{\partial v}{\partial Z'} \end{bmatrix} = - \begin{bmatrix} \frac{f_x}{Z'} & 0 & -\frac{f_x X'}{Z'^2} \\ 0 & \frac{f_y}{Z'} & -\frac{f_y Y'}{Z'^2} \end{bmatrix} \quad (8)$$

For the second part, we can obtain the following results through the Lie algebra perturbation model:

$$\frac{\partial P'}{\partial \delta \xi} = \frac{\partial TP}{\partial \delta \xi} \Rightarrow [I \quad -P'^{\wedge}] \quad (9)$$

, where $[\cdot]^{\wedge}$ denotes the skew-symmetric matrix of a vector. So, the Jacobian of point re-projection error can be constructed as (10).

$$J_p = \frac{\partial e_i^p}{\partial \delta \xi} = \frac{\partial e_i^p}{\partial P'} \frac{\partial P'}{\partial \delta \xi} = - \begin{bmatrix} \frac{f_x}{Z'} & 0 & -\frac{f_x X'}{Z'^2} & -\frac{f_x X' Y'}{Z'^2} & f_x + \frac{f_x X'^2}{Z'^2} & -\frac{f_x Y'}{Z'} \\ 0 & \frac{f_y}{Z'} & -\frac{f_y Y'}{Z'^2} & -f_y - \frac{f_y Y'^2}{Z'^2} & \frac{f_y X' Y'}{Z'^2} & \frac{f_y X'}{Z'} \end{bmatrix} \quad (10)$$

More detailed information can be found in [3] [16].

2) *Jacobian of line vertical errors*: We divided the re-projection error of line features e_l into horizontal e_{l_h} and vertical e_{l_v} , i.e. $e_l = e_{l_h} + e_{l_v}$. Vertical re-projection error is similar to the expression in [15] [27], and can be defined as (5). Firstly, we converted the 3D line L_w from the world frame to the current camera frame as follows:

$$L_c = \begin{bmatrix} \mathbf{n}_c \\ \mathbf{d}_c \end{bmatrix} = T_{cw} L_w = \begin{bmatrix} R_{cw} & (t_{cw})^{\wedge} R_{cw} \\ 0 & R_{cw} \end{bmatrix} L_w \quad (11)$$

, where the R_{cw} and t_{cw} represent the rotation matrix and translation vector from the world frame to the camera frame, respectively.

Then, the 3D line was projected into the image and described as l' , according to the known intrinsic parameter matrix of the camera, the projection of 3D line L_c from the camera frame to normalize image plane can be shown as follows:

$$l' = \mathcal{K} L_c = \begin{bmatrix} f_y & 0 & 0 \\ 0 & f_x & 0 \\ -f_y c_x & -f_x c_y & f_x f_y \end{bmatrix} \mathbf{n}_c = \begin{bmatrix} l_1 \\ l_2 \\ l_3 \end{bmatrix} \quad (12)$$

, where \mathcal{K} represents the projection matrix of the line. Note that the coordinates of the segment projected by the 3D line are

only related to the normal vector \mathbf{n}_c . Since we projected the line features into the image as an infinite line, only normal components \mathbf{n}_c in the *Plücker* coordinates L_c can provide meaningful information in the projection.

The vertical re-projection error of the line features can be expressed as follows, as mentioned in Section IV-A.

$$e_j^{l_v} = \begin{bmatrix} d_s \\ d_e \end{bmatrix} = \begin{bmatrix} \frac{\mathbf{p}_s^T \mathbf{l}'}{\sqrt{l_1'^2 + l_2'^2}} \\ \frac{\mathbf{p}_e^T \mathbf{l}'}{\sqrt{l_1'^2 + l_2'^2}} \end{bmatrix} \quad (13)$$

We assumed $l = \sqrt{l_1'^2 + l_2'^2}$ and $d = \frac{\mathbf{p}^T \mathbf{l}'}{l}$. So the Jacobian of vertical re-projection error of line feature can be expressed as:

$$\begin{aligned} \frac{\partial d}{\partial \delta \xi} &= \frac{\partial \mathbf{p}^T \mathbf{l}'}{\partial \delta \xi} \\ &= \frac{\partial (u l_1 + v l_2 + l_3) \frac{1}{l}}{\partial \delta \xi} \\ &= [l_1 \quad l_2] \frac{\partial \begin{bmatrix} u \\ v \end{bmatrix}}{\partial \delta \xi} \frac{1}{l} \end{aligned} \quad (14)$$

The following equation can be found using the chain rule:

$$\frac{\partial \begin{bmatrix} u \\ v \end{bmatrix}}{\partial \delta \xi} = \frac{\partial \begin{bmatrix} u \\ v \end{bmatrix}}{\partial P'} \frac{\partial P'}{\partial \delta \xi} \quad (15)$$

Finally, the Jacobian of the vertical re-projection error of the line features can be found by referring to the (10) as follows:

$$\begin{aligned} \frac{\partial d}{\partial \delta \xi} &= - [l_1 \quad l_2] \\ &\begin{bmatrix} \frac{f_x}{Z'} & 0 & -\frac{f_x X'}{Z'^2} & -\frac{f_x X' Y'}{Z'^2} & f_x + \frac{f_x X'^2}{Z'^2} & -\frac{f_x Y'}{Z'} \\ 0 & \frac{f_y}{Z'} & -\frac{f_y Y'}{Z'^2} & -f_y - \frac{f_y Y'^2}{Z'^2} & \frac{f_y X' Y'}{Z'^2} & \frac{f_y X'}{Z'} \end{bmatrix} \frac{1}{l} \end{aligned} \quad (16)$$

$$J_{l_v} = d_s \frac{\partial d_s}{\partial \delta \xi} + d_e \frac{\partial d_e}{\partial \delta \xi} \quad (17)$$

Compared to the methods of directly deriving the Lie algebra of the transformation in [3] [16], obtaining the Jacobian of vertical re-projection of the line features is more efficient and convenient over using the derivation result of the endpoints of the line.

3) *Jacobian of line horizontal errors*: The Jacobian derivation of the horizontal re-projection errors of the line feature was similar to the expression above. We defined the re-projection error of the matched and projected line midpoints as the cost function of line horizontal re-projection error. The result was shown as the following:

$$\frac{\partial e_k^{l_h}}{\partial \delta \xi} = \frac{\partial e_k^{l_h}}{\partial P'_m} \frac{\partial P'_m}{\partial \delta \xi} \quad (18)$$

, where P'_m represents 3D midpoint of matched line feature from previous frame to current camera frame.

Referring to (10), we can obtain the Jacobian of line feature horizontal re-projection error as follows:

$$\begin{aligned} J_{l_h} &= \frac{\partial e_k^{l_h}}{\partial \delta \xi} \\ &= - \begin{bmatrix} \frac{f_x}{Z'_m} & 0 & -\frac{f_x X'_m}{Z'^2_m} & -\frac{f_x X'_m Y'_m}{Z'^2_m} & f_x + \frac{f_x X'^2_m}{Z'^2_m} & -\frac{f_x Y'_m}{Z'_m} \\ 0 & \frac{f_y}{Z'_m} & -\frac{f_y Y'_m}{Z'^2_m} & -f_y - \frac{f_y Y'^2_m}{Z'^2_m} & \frac{f_y X'_m Y'_m}{Z'^2_m} & \frac{f_y X'_m}{Z'_m} \end{bmatrix} \end{aligned} \quad (19)$$

So far, the Jacobians of all three feature re-projection errors had been obtained, and we can obtain the pose transformation between adjacent frames by solving the non-linear least-square equation by Levenberg-Marquard algorithm.

V. EXPERIMENTAL RESULTS AND ANALYSIS

In this section, we will evaluate the proposed method on the public KITTI dataset [33] and EuRoC MAV dataset [34]. To verify the performance of our method, we compared the accuracy of our algorithm with the state-of-the-art VO systems that can run with stereo RGB data. The selected methods were stvo_pl [27], ORB_SLAM2 [6] and BoPLW [35]. In order to fairly compare all methods, we only kept the front end of ORB_SLAM2 and BoPLW to form VO systems. In addition, to illustrate the benefits of the line feature horizontal re-projection error on the accuracy of motion estimation, we showed the results of our proposal with only horizontal or vertical re-projection errors. Finally, we evaluated the ability of dynamic grids to cope with dynamic scenes on highly dynamic sequences, where the trajectory of a stereo camera in several video sequences with moving objects was estimated.

All the experiments had been run on an Intel Core i5-4210U CPU @ 1.70GHz \times 4 and 16 GB RAM without GPU. Since there are no dynamic objects in the EuRoC MAV dataset, we only estimated the trajectory of our method with or without dynamic grids in the KITTI dataset.

A. KITTI

We had tested the proposed method on the well-known KITTI dataset, which provided ground truth trajectories based on a 64 channel Velodyne LiDAR sensor and a GPS localization system. The stereo images were captured by two grayscale cameras (FL2-14S3M-C) attached to the top of a car. Since this dataset has highly textured urban scenes with light changes, it is close to the real autonomous driving scenes, and the dynamic scenes containing moving objects like cars and pedestrians in some image sequences have a great impact on the performance of the VO/vSLAM systems. To verify that the proposed method has an outstanding performance on accuracy, we showed both absolute pose error in table I and relative pose error in table II, together with three other systems, i.e. stvo_pl, ORB_SLAM2 front end, and BoPLW front end. On one hand, in table I with absolute pose error comparisons, we listed the root-mean-square error (RMSE) of absolute translation errors and rotation errors for the proposed method and the benchmark approaches, where our method had a better performance over other methods in 9 sequences and DynPL-SVO improved accuracy average 17.5%. The result

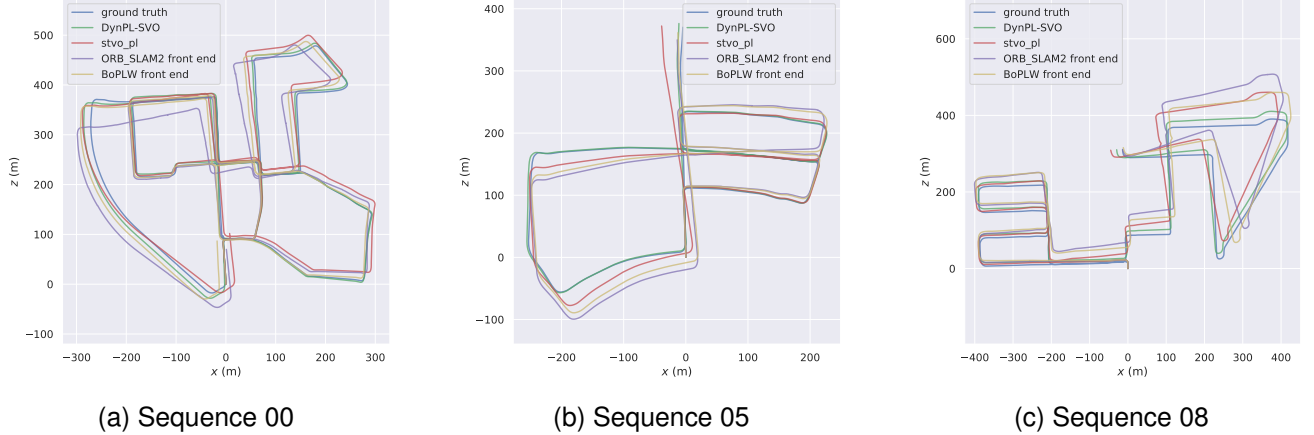


Fig. 3. Reconstruction of the path from DynPL-SVO, stvo_pl and ORB_SLAM2 front end. The ground truth was represented with blue lines, the green lines represented the estimation of our method, the red lines represented the estimation of stvo_pl, the path provided by ORB_SLAM2 and BoPLW are plotted with purple and brown lines, respectively. (a) Top view of the Sequence 00 path. (b) Top view of the Sequence 05 path. (c) Top view of the Sequence 08 path.

TABLE I
MEAN ABSOLUTE RMSE IN THE KITTI DATASET, NOTE THAT THE DASH INDICATES THAT THE EXPERIMENT FAILED.

Seq.	DynPL-SVO		stvo_pl		ORB_SLAM2 front end		BoPLW front end	
	t_m	R_{deg}	t_m	R_{deg}	t_m	R_{deg}	t_m	R_{deg}
00	6.691	1.788	7.426	2.105	14.076	3.461	7.551	1.519
01	172.502	8.910	371.245	12.212	-	-	-	-
02	21.653	4.423	8.167	1.505	14.187	2.615	11.276	2.550
03	6.077	4.308	6.030	3.310	2.317	1.511	3.018	1.466
04	2.100	29.944	2.216	34.067	2.655	49.025	2.550	38.861
05	4.097	1.598	6.506	2.695	11.755	4.217	8.750	3.641
06	4.113	2.927	5.564	6.305	4.219	1.518	4.120	2.364
07	5.216	1.957	3.028	2.165	14.155	5.698	15.512	6.957
08	7.202	3.019	10.054	3.254	24.796	6.134	17.134	3.302
09	4.729	1.065	12.205	2.454	18.387	3.718	24.154	4.288
10	2.064	1.831	2.649	1.155	3.823	2.081	4.992	1.823

showed that our method presented better accuracy performance in terms of motion estimation in most sequences, especially in the dynamic ones. On the other hand, in table II with relative pose errors comparisons, the result showed that our system achieve better accuracy over other comparative experimental systems in most scenes. Figure 3 showed the reconstruction of the path from DynPL-SVO, stvo_pl, ORB_SLAM2 front end and BoPLW front end on several sequences of the KITTI dataset where dynamic objects and a lot of challenging scenes presented. It is observed that the reconstructed paths from compared systems had larger deviation than the proposed approach in all experimental sequences, especially around corners with large point of view changes. This mean that the proposed method obtained more accurate absolute solutions than other experimental systems in dealing with challenging and dynamic environments, attribute to the introduced dynamic grids and the horizontal re-projection error into the proposed method.

We further compared our approach with BoPLW on the KITTI dataset. The BoPLW is a visual SLAM approach to expand from ORB_SLAM2 with line features. As shown in table I, our method had higher accuracy values than BoPLW in most sequences. As an illustrative example, Figure 4 showed the distribution of the features during motion estimation on



Fig. 4. Picture from *KITTI-01*. The green points represented point features and green lines represented line features. There were many features attached to the moving cars reducing the robustness of the system.

KITTI-01. There are large numbers of dynamic objects, such as moving cars in the dataset scene. DynPL-SVO outperformed other methods in the dynamic environment. One of the reasons is the use of dynamic grids to remove the dynamic point features. It was emphatic that, a lot of features on dynamic objects were used to estimate the motion of the camera, in the benchmark method resulting in error estimation. Eventually, the task execution failed due to the insufficient number of stable features, such as the ORB_SLAM2 and BoWPL front end shown in table I and table II. The line feature introduction ensured that DynPL-SVO and stvo_pl can run stably in all scenes, and the additional horizontal errors of the line features make DynPL-SVO achieve better accuracy than stvo_pl.

TABLE II
MEAN RELATIVE POSE ERRORS ON THE KITTI DATASET, NOTE THAT THE DASH INDICATES THAT THE EXPERIMENT FAILED.

Seq.	DynPL-SVO		stvo_pl		ORB_SLAM2 front end		BoPLW front end	
	t%	R _{deg/100m}	t%	R _{deg/100m}	t%	R _{deg/100m}	t%	R _{deg/100m}
00	1.569	0.443	1.607	0.405	1.424	0.590	1.137	0.366
01	21.339	1.402	43.723	1.939	-	-	-	-
02	1.733	0.517	1.738	0.344	1.621	0.508	1.581	0.433
03	3.604	1.637	3.467	1.260	1.964	0.712	2.140	0.639
04	1.907	0.424	2.023	0.282	2.447	0.498	3.398	0.511
05	1.007	0.375	1.412	0.493	2.649	0.754	2.405	0.609
06	1.898	0.582	2.372	0.506	1.974	0.524	1.761	0.567
07	2.051	0.879	1.725	1.047	4.658	2.138	5.067	2.542
08	1.279	0.453	1.670	0.468	3.121	0.959	2.642	0.608
09	1.486	0.353	2.129	0.465	3.422	1.044	4.388	0.933
10	1.204	0.572	1.032	0.337	1.693	0.716	1.903	0.566

TABLE III
MEAN ABSOLUTE AND RELATIVE RMSE ERRORS ON THE KITTI DATASET.

Seq.	wo/line error		w/vertical error		w/horizontal error	
	APE	RPE	APE	RPE	APE	RPE
00	7.3728	0.0323	11.9514	0.0391	6.6818	0.0322
01	52.5071	0.7188	166.6740	1.0059	89.8455	0.7788
02	20.6018	0.0348	23.6016	0.0559	19.5024	0.0346
03	6.2301	0.0317	6.0842	0.0322	6.2207	0.0317
04	2.7768	0.0374	2.2843	0.0554	2.7410	0.0365
05	3.9010	0.0182	4.3099	0.0196	3.8735	0.0181
06	5.0703	0.0326	4.6390	0.0448	4.9705	0.0322
07	1.5365	0.0178	5.4844	0.0634	1.8679	0.0174
08	5.4780	0.0390	7.3161	0.0441	4.8398	0.0389
09	4.5855	0.0248	4.4380	0.0674	4.5637	0.0245
10	2.0184	0.0198	2.2578	0.0342	2.0173	0.0197

Finally, we did an ablation study on different directions of line features in our system, yielding the results presented in table III. We can observe that the system with only the horizontal error has more accurate results than the one only with the vertical errors in almost all sequences of the KITTI dataset, especially on relative errors. The horizontal re-projection error helped achieves better accuracy in 10 sequences over the system without a line error and improves the accuracy by 49.1% compared to the vertical re-projection error in the KITTI dataset. Figure 5 depicted the matching results of line features between adjacent frames in the sequence KITTI-03. It even was noted that there are still enough stable line features even in challenging scenes. The numerous short lines indicated more superior characteristics in horizontal re-projection errors over vertical ones, causing the system with horizontal re-projection errors to have a better performance in most sequences, especially in relative errors.

B. EuRoC MAV

The EuRoC MAV dataset, which was collected by a micro aerial vehicle (MAV), included 11 sequences in two indoor scenes. The dataset contains stereo images from a global shutter camera (Aptina MT9V034 global shutter, WVGA monochrome, and 20 FPS) and a synchronized inertial measurement unit (IMU, ADIS16448, 200 Hz) [2]. Note that the dataset is an indoor dataset with large rotation movements of drones, where there are a lot of line features in the indoor environment for motion estimation. We ran DynPL-

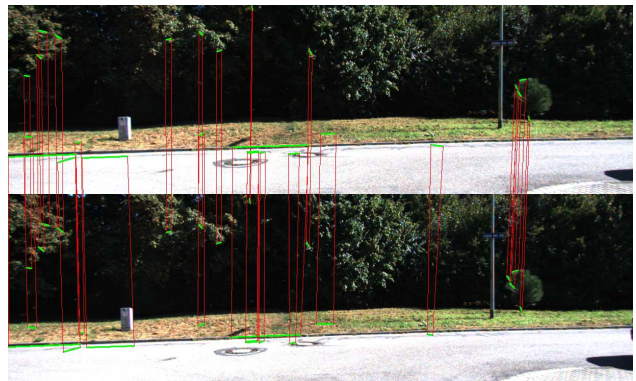


Fig. 5. The matching results of line features between adjacent frames in challenging scenes on KITTI-03. The line features were represented with green lines and the match lines were represented with red lines. There were still enough stable line features even in challenging scenes with the help of horizontal re-projection errors to improve pose estimation.

SVO and stvo_pl for comparison. In addition, to verify that the horizontal re-projection errors of the line features have an optimized effect on estimation accuracy, we also ran the method with only horizontal or vertical re-projection errors, respectively, on the EuRoC MAV dataset.

As an example, Figure 6(a) showed the line features extraction in the V2_01_easy sequence, Figure 6(b) and 6(c) showed the line features before and after the optimization process in the motion estimation, respectively. There were a large amount of short but complete lines in the scene, as mentioned above, where horizontal re-projection errors showed more superior characteristics in this case over the vertical re-projection errors. At the same time, we observed good performance of all line features by minimizing re-projection errors. Table IV showed that the systems with horizontal re-projection error, i.e. our system and the system with only horizontal error, provided more accurate results in 9 experimental scenes of the EuRoC MAV dataset, even in the indoor and static environment. The ablation study showed that the horizontal error played a more important roles than the vertical error in most sequences, and DynPL-SVO also had higher accuracy than stvo_pl, such as MH_01_easy, MH_04_different etc. This attributed to the fact that there were many short but complete lines in the sequences and the use of horizontal re-projection errors in DynPL-SVO helped improve the performance. This

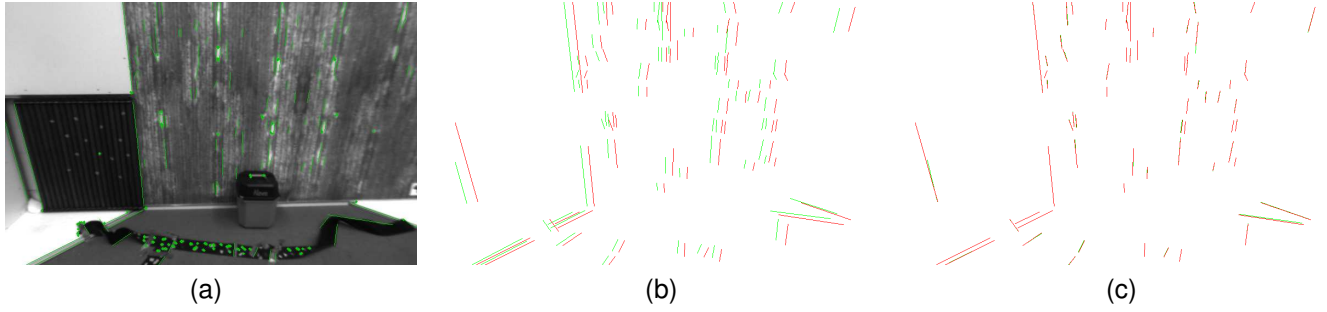


Fig. 6. The tracking of line features in the process of motion estimation. (a) result of features detection on V2_01_easy. (b) line features before pose optimization, the green lines represented detected line segments from the current frame, and the red lines represented re-projected line segments from the previous frame. (c) results of motion estimation. There were also numerous stable short line features in indoor scenes, efficient for optimization by horizontal re-projection errors.

TABLE IV
MEAN RELATIVE RMSE ON THE EUROC MAV DATASET.

Sequence	stvo_pl	DynPL-SVO	DynPL-SVO w/vertical error	DynPL-SVO w/horizontal error
MH_01_easy	0.033349	0.033276	0.033294	0.033358
MH_02_easy	0.032896	0.032547	0.032501	0.032016
MH_03_med	0.073692	0.072181	0.071908	0.071196
MH_04_dif	0.103936	0.103109	0.103346	0.103473
MH_05_dif	0.095603	0.094194	0.094640	0.094608
V1_01_easy	0.048642	0.049194	0.049011	0.049427
V1_02_med	0.102017	0.102235	0.102260	0.101900
V1_03_dif	0.098576	0.101252	0.101670	0.097804
V2_01_easy	0.037155	0.032626	0.032655	0.032629
V2_02_med	0.074001	0.071558	0.073592	0.071348

experiment proved that the horizontal re-projection errors had an important role in motion estimation performance, and even more than the contributed of the vertical re-projection errors. Besides, DynPL-SVO can also provide a good result in a static environment.

C. Evaluation of the ability of dynamic grids to cope with dynamic scenes.

By combining the dynamic grid method with the VO system, the ability of the system to deal with dynamic scenes can also be improved. A comparative analysis was done to determine the improvement of dynamic grids in a series of dynamic sequences. There are moving objects like cars and people in the KITTI dataset. Figure 7(a) and Figure 7(b) showed that the dynamic grids can identify vehicles traveling at high speeds in different directions, regardless of whether the scene contained rich structural information. In addition, for dynamic objects moving slowly, such as pedestrians, the dynamic grids can still eliminate dynamic features through the complete market area (shown in Figure 7(c) and (d)). It verified that the dynamic grids can accurately identify the dynamic regions to avoid the influence of dynamic features on the accuracy, and DynPL-SVO was robust in dynamic scenes. To represent the error in the quantitative analysis, we compared the absolute and relative root-mean-square error (RMSE) with and without dynamic grid approaches in the KITTI dataset, as shown in table V. It can be noticed that the system with the dynamic grid method had more accurate estimation in 8 sequences and enhanced accuracy by about 15% compared to the traditional approaches. Especially, the

TABLE V
MEAN ABSOLUTE AND RELATIVE RMSE ERRORS IN KITTI DATASET.

Seq.	DynPL-SVO w/dynamic grid		DynPL-SVO wo/dynamic grid	
	APE	RPE	APE	RPE
00	11.221715	0.040752	13.236462	0.038351
01	182.531449	1.019784	319.707988	1.306922
02	21.654051	0.064572	10.960957	0.055898
03	6.094158	0.032278	5.946504	0.031802
04	2.207623	0.054315	2.015523	0.052209
05	4.403628	0.019534	7.060361	0.019145
06	4.428359	0.044869	4.440736	0.056673
07	5.216922	0.062928	4.725139	0.064078
08	7.443639	0.043877	12.509229	0.042731
09	4.823906	0.066494	13.612393	0.070549
10	2.282632	0.032286	2.786268	0.033558

dynamic grid method worked well in sequences with highly dynamic scenes (such as KITTI-01,05,09), even improved accuracy by more than 30%. However, when there were large numbers of unstable scenes in the surrounding environment, such as the KITTI-02 with the presence of a large number of non-artificial environments and the lack of dynamic objects, the accuracy of the results estimated by our method degraded. The main reason is that the dynamic grids marked some unstable positions like leaves as dynamic regions, reducing the number of features involved in motion estimation and the accuracy of the results. The results proved that DynPL-SVO gave more stable and higher accuracy motion estimation in a dynamic environment.

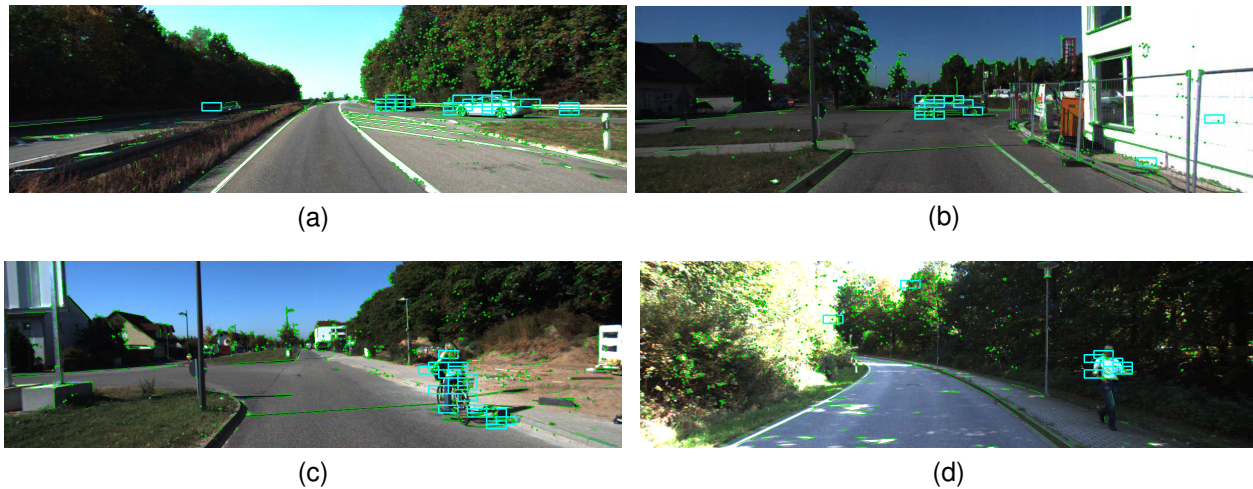


Fig. 7. Dynamic scenes on the *KITTI* dataset and the effect of dynamic grids on dynamic regions. The blue boxes represent the dynamic grids. (a) Moving cars in *KITTI-01*. (b) Moving car in *KITTI-06*. (c) The person riding a bike in *KITTI-06*. (d) The pedestrian in *KITTI-09*.

VI. CONCLUSIONS

In this paper, a robust RGB stereo visual odometry method using both point and line features, i.e., DynPL-SVO, was proposed in dynamic scenes. In order to cope with the reduction of robustness and accuracy of visual odometry systems induced by dynamic objects, the *dynamic grid* method that can efficiently mark dynamic regions and remove point features on dynamic objects without using depth information and other sensors was also proposed. In addition, to make full use of the structural information of line features, the horizontal re-projection error of the line features was introduced into the cost function to further improve the motion estimation accuracy. Finally, DynPL-SVO was compared with three different systems, such as stvo_pl, ORB_SLAM2 front end, and BoPLW front end on two different datasets, i.e., KITTI and EuRoC MAV. The experimental results showed that DynPL-SVO can produce a more robust and accurate results in most scenes, especially in dynamic ones.

Future work will focus on introducing features with more geometric information, such as planes and cubes, into the system to further improve the accuracy of estimation and create a more informative map. Lastly, using deep learning to improve the ability of the system to deal with dynamic scenes is also a promising direction.

REFERENCES

- [1] T. Qin, P. Li, S. Shen, Vins-mono: A robust and versatile monocular visual-inertial state estimator, *IEEE Transactions on Robotics* 34 (4) (2018) 1004–1020.
- [2] Z. Liu, D. Shi, R. Li, W. Qin, Y. Zhang, X. Ren, Plc-vio: Visual-inertial odometry based on point-line constraints, *IEEE Transactions on Automation Science and Engineering* (2021).
- [3] Y. He, J. Zhao, Y. Guo, W. He, K. Yuan, Pl-vio: Tightly-coupled monocular visual-inertial odometry using point and line features, *Sensors* 18 (4) (2018) 1159.
- [4] R. Sahdev, B. X. Chen, J. K. Tsotsos, Indoor localization in dynamic human environments using visual odometry and global pose refinement, in: 2018 15th Conference on Computer and Robot Vision (CRV), IEEE, 2018, pp. 360–367.
- [5] M. Ouyang, Z. Cao, P. Guan, Z. Li, C. Zhou, J. Yu, Visual-gyroscope-wheel odometry with ground plane constraint for indoor robots in dynamic environment, *IEEE Sensors Letters* 5 (3) (2021) 1–4.
- [6] R. Mur-Artal, J. D. Tardós, Orb-slam2: An open-source slam system for monocular, stereo, and rgb-d cameras, *IEEE transactions on robotics* 33 (5) (2017) 1255–1262.
- [7] B. Kitt, A. Geiger, H. Lategahn, Visual odometry based on stereo image sequences with ransac-based outlier rejection scheme, in: 2010 IEEE intelligent vehicles symposium, IEEE, 2010, pp. 486–492.
- [8] E. Rublee, V. Rabaud, K. Konolige, G. Bradski, Orb: An efficient alternative to sift or surf, in: 2011 International conference on computer vision, Ieee, 2011, pp. 2564–2571.
- [9] D. G. Lowe, Distinctive image features from scale-invariant keypoints, *International journal of computer vision* 60 (2) (2004) 91–110.
- [10] R. G. Von Gioi, J. Jakubowicz, J.-M. Morel, G. Randall, Lsd: A fast line segment detector with a false detection control, *IEEE transactions on pattern analysis and machine intelligence* 32 (4) (2008) 722–732.
- [11] L. Zhang, R. Koch, An efficient and robust line segment matching approach based on lbd descriptor and pairwise geometric consistency, *Journal of Visual Communication and Image Representation* 24 (7) (2013) 794–805.
- [12] J. Sola, T. Vidal-Calleja, J. Civera, J. M. M. Montiel, Impact of landmark parametrization on monocular ekf-slam with points and lines, *International journal of computer vision* 97 (3) (2012) 339–368.
- [13] X. Luo, Z. Tan, Y. Ding, Accurate line reconstruction for point and line-based stereo visual odometry, *IEEE Access* 7 (2019) 185108–185120.
- [14] A. Bartoli, P. Sturm, Structure-from-motion using lines: Representation, triangulation, and bundle adjustment, *Computer vision and image understanding* 100 (3) (2005) 416–441.
- [15] R. Gomez-Ojeda, F.-A. Moreno, D. Zuniga-Noël, D. Scaramuzza, J. Gonzalez-Jimenez, Pl-slam: A stereo slam system through the combination of points and line segments, *IEEE Transactions on Robotics* 35 (3) (2019) 734–746.
- [16] X. Zuo, X. Xie, Y. Liu, G. Huang, Robust visual slam with point and line features, in: 2017 IEEE/RSJ International Conference on Intelligent Robots and Systems (IROS), IEEE, 2017, pp. 1775–1782.
- [17] A. Pumarola, A. Vakhitov, A. Agudo, A. Sanfeliu, F. Moreno-Noguer, Pl-slam: Real-time monocular visual slam with points and lines, in: 2017 IEEE international conference on robotics and automation (ICRA), IEEE, 2017, pp. 4503–4508.
- [18] C. Kerl, J. Sturm, D. Cremers, Robust odometry estimation for rgb-d cameras, in: 2013 IEEE international conference on robotics and automation, IEEE, 2013, pp. 3748–3754.
- [19] T. Whelan, H. Johannsson, M. Kaess, J. J. Leonard, J. McDonald, Robust real-time visual odometry for dense rgb-d mapping, in: 2013 IEEE International Conference on Robotics and Automation, IEEE, 2013, pp. 5724–5731.
- [20] J. Engel, T. Schöps, D. Cremers, Lsd-slam: Large-scale direct monocular slam, in: European conference on computer vision, Springer, 2014, pp. 834–849.
- [21] J. Engel, V. Koltun, D. Cremers, Direct sparse odometry, *IEEE transactions on pattern analysis and machine intelligence* 40 (3) (2017) 611–625.

- [22] G. Zhang, J. H. Lee, J. Lim, I. H. Suh, Building a 3-d line-based map using stereo slam, *IEEE Transactions on Robotics* 31 (6) (2015) 1364–1377.
- [23] R. Gomez-Ojeda, J. Briales, J. Gonzalez-Jimenez, Pl-svo: Semi-direct monocular visual odometry by combining points and line segments, in: 2016 IEEE/RSJ International Conference on Intelligent Robots and Systems (IROS), IEEE, 2016, pp. 4211–4216.
- [24] J. H. Lee, S. Lee, G. Zhang, J. Lim, W. K. Chung, I. H. Suh, Outdoor place recognition in urban environments using straight lines, in: 2014 IEEE International Conference on Robotics and Automation (ICRA), IEEE, 2014, pp. 5550–5557.
- [25] C. Akinlar, C. Topal, Edlines: A real-time line segment detector with a false detection control, *Pattern Recognition Letters* 32 (13) (2011) 1633–1642.
- [26] T. Koletschka, L. Puig, K. Daniilidis, Mevo: Multi-environment stereo visual odometry, in: 2014 IEEE/RSJ International Conference on Intelligent Robots and Systems, IEEE, 2014, pp. 4981–4988.
- [27] R. Gomez-Ojeda, J. Gonzalez-Jimenez, Robust stereo visual odometry through a probabilistic combination of points and line segments, in: 2016 IEEE International Conference on Robotics and Automation (ICRA), IEEE, 2016, pp. 2521–2526.
- [28] T. Zhu, H. Ma, Challenges of dynamic environment for visual-inertial odometry, in: 2018 3rd International Conference on Robotics and Automation Engineering (ICRAE), IEEE, 2018, pp. 82–86.
- [29] H. Kim, P. Kim, H. J. Kim, Moving object detection for visual odometry in a dynamic environment based on occlusion accumulation, in: 2020 IEEE International Conference on Robotics and Automation (ICRA), IEEE, 2020, pp. 8658–8664.
- [30] D.-H. Kim, J.-H. Kim, Effective background model-based rgb-d dense visual odometry in a dynamic environment, *IEEE Transactions on Robotics* 32 (6) (2016) 1565–1573.
- [31] Q. Sun, Y. Tang, C. Zhang, C. Zhao, F. Qian, J. Kurths, Unsupervised estimation of monocular depth and vo in dynamic environments via hybrid masks, *IEEE Transactions on Neural Networks and Learning Systems* (2021).
- [32] Y. Wan, W. Gao, S. Han, Y. Wu, Dynamic object-aware monocular visual odometry with local and global information aggregation, in: 2020 IEEE International Conference on Image Processing (ICIP), IEEE, 2020, pp. 603–607.
- [33] A. Geiger, P. Lenz, C. Stiller, R. Urtasun, Vision meets robotics: The kitti dataset, *The International Journal of Robotics Research* 32 (11) (2013) 1231–1237.
- [34] M. Burri, J. Nikolic, P. Gohl, T. Schneider, J. Rehder, S. Omari, M. W. Achtelik, R. Siegwart, The euroc micro aerial vehicle datasets, *The International Journal of Robotics Research* 35 (10) (2016) 1157–1163.
- [35] K. Qian, W. Zhao, K. Li, X. Ma, H. Yu, Visual slam with boplw pairs using egocentric stereo camera for wearable-assisted substation inspection, *IEEE Sensors Journal* 20 (3) (2019) 1630–1641.